

# A Survey of Cardiac 4D PC-MRI Data Processing

B. Köhler<sup>1</sup>, S. Born<sup>2</sup>, R. F. P. van Pelt<sup>3</sup>, U. Preim<sup>4</sup>, B. Preim<sup>1</sup>

<sup>1</sup>Department of Simulation and Graphics, Otto-von-Guericke University, Magdeburg, Germany

<sup>2</sup>Department of Surgical Research, University of Zürich, Switzerland

<sup>3</sup>Department of Image Guided Therapy Systems, Philips Healthcare, Best, The Netherlands & Yacht, Eindhoven, The Netherlands

<sup>4</sup>Department of Diagnostic Radiology, Municipal Hospital, Magdeburg, Germany

ben.koehler@isg.cs.uni-magdeburg.de

---

## Abstract

*Cardiac 4D PC-MRI acquisitions gained increasing clinical interest in recent years. They allow to non-invasively obtain extensive information about patient-specific hemodynamics and thus have a great potential to improve the diagnosis of cardiovascular diseases. A dataset contains time-resolved, three-dimensional blood flow directions and strengths, facilitating comprehensive qualitative and quantitative data analysis. The quantification of measures such as stroke volumes helps to assess the cardiac function and monitor disease progression. Qualitative analysis allows to investigate abnormal flow characteristics, such as vortices, that are correlated to different pathologies. Processing the data comprises complex image processing methods as well as flow analysis and visualization. In this work, we mainly focus on the aorta. We provide an overview from data measurement and preprocessing to current visualization and quantification methods so that other researchers can quickly catch up with the topic and take on new challenges to further investigate the potential of 4D PC-MRI.*

Categories and Subject Descriptors (according to ACM CCS): I.4.9 [Computing Methodologies]: Image Processing and Computer Vision—Applications J.3 [Computing Applications]: Life and Medical Sciences—

---

## 1 Introduction

Information about blood flow in the heart and its surrounding vessels can improve the diagnosis of cardiovascular diseases (CVDs). 2D phase-contrast magnetic resonance imaging (PC-MRI) acquisitions became a useful tool in the clinical routine to measure regional blood flow in one slice that is angulated prior to the scan. A heart valve's function can be assessed by quantifying *flow rates* and determining if there is significant back flow (*regurgitation fraction*). The pumped blood per heartbeat (*stroke volume*) is used to evaluate the heart's pumping capacity. Increased *peak flow velocities* may occur in narrowed (*stenotic*) vessels.

Technical progress in the field of MRI nowadays enables 4D PC-MRI acquisitions (also: *flow-sensitive MRI*, *MR velocity mapping*). This was introduced by Wigström et al. [WSW96] and is able to provide time-resolved 3D velocity fields. These data allow an extensive quantification, since measuring planes can flexibly be adjusted *after* the scan. Further possible measures such as *pulse wave velocities* and *wall shear stress* are correlated to vessel stiffness and pathologic dilation (*aneurysm*), respectively. In addition, a quali-

tative analysis of the pulsatile blood flow becomes possible. Characteristic flow aspects facilitate a deeper understanding of a patient's situation, since specific patterns such as vortex flow are correlated to different pathologies. There is, e.g., a high probability of emerging systolic vortex flow in the ascending aorta if the aortic valve is *bicuspid*, i.e., two of the three leaflets are fused, which affects the valve's opening characteristics. Vortex flow close to the vessel wall may induce high shear forces that, in turn, increase the risk of aneurysm development. Further understanding this mutual influence of hemodynamics and vessel morphology can support treatment decision-making and the corresponding risk assessment. Advances towards higher resolution and faster acquisitions, as well as studies proving the clinical impact, yielded an increasing interest in 4D PC-MRI in recent years [CRvdG\*14, MKE11, SAG\*14].

**Organization.** Sec. 2 explains 4D PC-MRI acquisitions and related artifacts. Vessel segmentation is described in Sec. 3. Sec. 4 characterizes methods to visualize the anatomical context. Qualitative and quantitative data analysis techniques are presented in Sec. 5 and 6. Sec. 7 concludes.

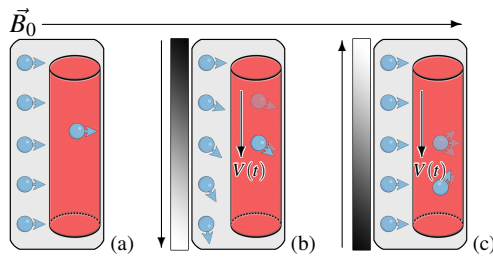


Figure 1: (a) The  $B_0$  magnetic field aligns all spins (blue) in stationary tissue (gray) as well as vessels (red). (b) A magnetic gradient field causes a position-dependent phase shift. (c) The inverted gradient removes the phase shifts in stationary tissue. Phase encodes the velocity  $V(t)$  in moving fluids. Images based on Lotz et al. [LMLG02].

## 2 Data Acquisition

A basic understanding of 4D PC-MRI is essential to develop new analysis methods. Thus, acquisition fundamentals and data characteristics are explained in the following.

### 2.1 4D PC-MRI Imaging

Atoms in the body precess around an internal axis (*spin*) with a specific angle (*phase*). The magnetization in MRI mainly affects the spins of hydrogen atoms from water molecules. This allows to distinguish water from fat tissue, but also to encode fluid movement. A magnetic field  $B_0$  aligns the phases with the  $B_0$  direction (Fig. 1a). A linear magnetic field gradient causes a phase shift depending on an atom's position (Fig. 1b). The application of the inverted gradient erases this effect in static tissue. In the moving blood, however, there is a measurable phase difference that is directly related to the flow velocity (Fig. 1c). A PC-P reconstruction, which calculates all phase differences, yields *phase* (also: *gradient, velocity*) images  $V_{\{x,y,z\}}$  with velocities, i.e., flow directions and strengths (Fig. 2a). There is each one image per patient-oriented xyz dimension. A PC-M reconstruction processes undirected flow strengths into three *magnitude* images  $M_{\{x,y,z\}}$ , which are less error-prone to uncorrelated noise (Fig. 2c). An anatomy image  $A$  is derived from averaging signal intensities (Fig. 2b). Some papers refer to this as magnitude image instead. Datasets contain a full heartbeat, which is the average of multiple cardiac cycles during several minutes. Typical resolutions are 1.5–2.5 [mm] between data points in a slice with slice distances of 2–4 [mm] and 20–50 [ms] between subsequent time steps. This yields a grid with about  $150 \times 200$  voxels in each of the 20–50 slices and 15–40 temporal positions.

The two bipolar magnetic field gradients are adjusted so that the maximum phase shifts of  $\pm 180^\circ$  correspond to the *velocity encoding* ( $V_{ENC}$ ). This essential scan parameter describes the maximum measurable blood flow velocity between  $\pm V_{ENC}$  [m/s] per dimension. Exploiting the full range is desired to obtain higher phase differences, resulting in increased image contrast. A common choice for aortic blood flow is 1.5 [m/s] [MFK\*12]. Flow velocities, e.g., in the ventricles or pathologically narrowed vessels, differ greatly.

Thus, focusing the scan on a specific vessel is crucial. Nett et al. [NJF\*12] describe a dual  $V_{ENC}$  approach that combines flow images with different  $V_{ENC}$  to cover a wide range of velocities (high  $V_{ENC}$ ) and still obtain a decent contrast (low  $V_{ENC}$ ). However, acquisition times increase and an image composition scheme is required.

### 2.2 Artifacts and Corrections

**Phase Unwrapping.** If a measured velocity value exceeds the  $V_{ENC}$ , it flips, which means that the measured flow seemingly runs in the opposite direction (Fig. 3a). Assuming that velocities of spatio-temporally adjacent voxels should not differ by more than  $V_{ENC}$ , such *phase wraps* can be identified and corrected [BKHM07, DR04] (Fig. 3b). Loecher et al. [LJLW11] use a probabilistic measure to decide if a voxel is phase wrapped. Salfity et al. [SHG\*06] compare the performance of phase unwrapping algorithms that consider one, three and four dimensions.

**Velocity Offset Correction.** Inhomogeneous or imbalanced magnetic field gradients cause a systematic, non-constant error, which can be subtracted from the image using a *velocity offset* (also: *phase offset, eddy current*) correction. Walker et al. [WCS\*93] calculate the standard deviation (*std*) for each voxel in the phase image along the temporal dimension. The temporal *std* is highest for air and lowest for static tissue; vessels are in between. Based on the assumption that obtained flow velocities in static tissue are erroneous, an approximate static tissue mask is created via interactive thresholding (Fig. 3c). One plane per phase image slice per temporal position is fitted to the velocity values of the static tissue mask (Fig. 3d) and then subtracted from the corresponding phase image slice. Bock et al. [BKHM07] suggest to fit only one plane in the late diastole, since here the aorta and pulmonary artery have the least motion, and use this for the correction of all time steps. Chernobelsky et al. [CSCW07] and Lankhaar et al. [LHM\*05] showed that such corrections improve quantification results. Fair et al. [FGG\*13] investigated improvements when using data with a higher signal-to-noise ratio. Lotz et al. [LMLG02] point out that phase offset corrections can also introduce new errors.

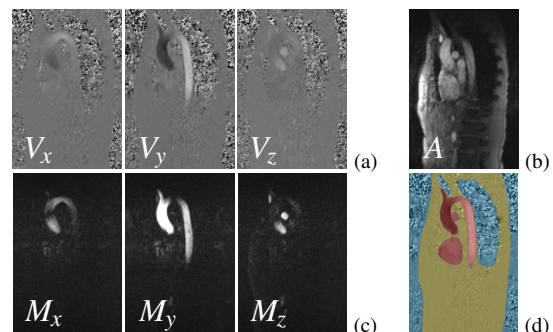


Figure 2: Thoracic images (seen from the side) of the aorta at a specific time point during the heart cycle. Phase (a), anatomy (b) and magnitude (c) images. (d) Labeling of the heart (red), body (yellow) and air (blue).

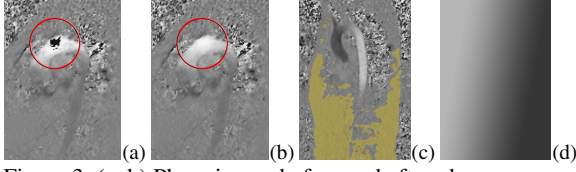


Figure 3: (a, b) Phase image before and after phase unwrapping. (c, d) Estimated static tissue mask (yellow) and fitted 2D gradient as phase offset approximation.

**Divergence Filtering.** Blood as an incompressible fluid should be divergence-free, which might not be the case in the acquired data due to measurement errors. *Divergence filters* suppress these divergent components. Ong et al. [OUT\*15] describe a technique based on wavelet transform that improves visualization while preserving quantification results and that is robust to segmentation errors. Bostan et al. [BVP\*13] additionally incorporate conditions about the flow’s rotational behavior and assume that flow varies smoothly over time. They introduced a flow field regularization that improved the visualization of helical patterns in 4D PC-MRI data of the aorta. However, a quantitative comparison was not performed. Thus, it is not clear if the calculation of quantitative measures remains reliable.

### 3 Vessel Segmentation

For many subsequent analysis and visualization tasks, a vessel segmentation or approximation is required. Lesage et al. [LABFL09] provide an overview of general 3D vessel segmentation techniques that are not tailored to cardiac vessels. Mirzaee et al. [MH15] fuse flow images with additional anatomical data to improve the segmentation, e.g., of stenotic vessels. In this section, we explain selected approaches that are solely using the 4D PC-MRI image data.

#### 3.1 Preprocessing: Contrast Enhancement

An automatic 4D segmentation is challenging, since image contrast depends on the time-varying blood flow velocities. Manual 4D segmentation of the whole vessel is not feasible in clinical practice due to the enormous expenditure of time. A common approach is to derive a 3D contrast-enhanced image, which no longer has temporal information.

A *temporal maximum intensity projection* (TMIP) obtains the maximum velocity per voxel along the temporal dimension of size  $N$ . Usually, this technique is applied to the magnitude images [VPBB\*10]. The TMIP is bright at positions  $\vec{p} \in \mathbb{R}^3$ , where fast blood flow was present at some time  $t = 0 \dots N-1$  during the cardiac cycle (Fig. 4a, Eq. 1). Inflow jets may appear prominently; distant vessel sections can lose contrast due to decreasing velocities. Further contrast variations might be caused by the typically parabolic flow profile, which means that the highest velocities are located in the center. This profile can be disturbed in case of vortex flow.

A *phase contrast magnetic resonance angiography* (PCMRA) image [HFS\*11] combines the anatomy with the phase images. Both have a high vessel contrast, but an opposing high and low contrast for static tissue and noise re-



(a) TMIP (b) PCMRA (c) LPC (d) EVC  
Figure 4: 3D images with enhanced vessel contrast.

gions. The PCMRA can be calculated using Eq. 2 or similar formulae [BWJ\*08]. A temporal average instead of the maximum is calculated (Fig. 4b).

Chung et al. [CNS04] define *local phase coherence* (LPC) as average angle between a normalized velocity vector and its normalized neighbors at  $\vec{p}_t^n$  (Eq. 3). The normalization causes insensitivity towards the actual velocities, which might be advantageous in vessels with slower blood flow or if the image contrast is poor due to a too high  $V_{ENC}$ . Temporal information are preserved, however, averaging along the temporal dimension (like in Eq. 2) is recommended (Fig. 4c). Similar to the LPC, Solem et al. [SPH04] describe *eigenvalue coherence* (EVC), which is based on an eigenvalue analysis of a local velocity tensor (Fig. 4d, Eq. 4).

$$\text{TMIP}(\vec{p}) = \max_t \left( \|M(\vec{p}_t)\| \right) \quad (1)$$

$$\text{PCMRA}(\vec{p}) = \frac{1}{N} \cdot \sum_{t=0}^{N-1} \|M(\vec{p}_t)\| \cdot \|V(\vec{p}_t)\| \quad (2)$$

$$\text{LPC}(\vec{p}_t) = \frac{1}{26} \cdot \sum_{\forall \vec{p}_t^n} \frac{V(\vec{p}_t) \cdot V(\vec{p}_t^n)}{\|V(\vec{p}_t)\| \cdot \|V(\vec{p}_t^n)\|} \quad (3)$$

$$\text{EVC}(\vec{p}_t) = \frac{4 \cdot \lambda_0 \cdot \lambda_1}{(\lambda_0 + \lambda_1)^2} \quad \text{with} \quad (4)$$

$$\{\lambda_0 \geq \lambda_1 \geq \lambda_2\} = \text{eig} \left( \frac{1}{26} \cdot \sum_{\forall \vec{p}_t^n} V(\vec{p}_t^n) \cdot V(\vec{p}_t^n)^T \right),$$

$$M(\vec{p}_t) = \begin{pmatrix} M_x(\vec{p}_t) \\ M_y(\vec{p}_t) \\ M_z(\vec{p}_t) \end{pmatrix} \quad \text{and} \quad V(\vec{p}_t) = \begin{pmatrix} V_x(\vec{p}_t) \\ V_y(\vec{p}_t) \\ V_z(\vec{p}_t) \end{pmatrix}$$

#### 3.2 3D Lumen Segmentation

A 3D vessel mask is an approximation of the dynamic vessel and can be used for the subsequent anatomical context visualization or for quantification purposes.

**Region-based Approaches.** Hennemuth et al. [HFS\*11] use a *watershed transformation* on a PCMRA image, where the user specifies include and exclude points. Stalder et al. [SGGJ13] cluster the temporal standard deviation image [WCS\*93] into air, static tissue and vessels. The method is fully automatic, but does not allow to distinguish between different vessels.

**Graph-based Approaches.** Köhler et al. [KPG\*15] use *graph cuts* on the TMIP, where regions in- and outside the vessel are user-provided via drawing. Gülsün et al. [GT10]

compute a centerline based on a *medialness map* between user-specified seeds on a PCMRA image and extract the vessel lumen using a graph cut with the centerline as input.

**Model-based Approaches.** Van Pelt et al. [VPNtHRV12] use an *active surface model* on the TMIP, where three parameters for internal and external forces of the energy minimization can be adjusted. Volonghi et al. [VTC\*15] estimate the vessel via thresholding on a PCMRA image filtered with anisotropic diffusion. An initial surface is extracted using marching cubes and a centerline is approximated. This is used as initialization for an automatic *level set* segmentation.

### 3.3 Cross-section Segmentation

Quantification methods often require an *accurate* definition of the lumen in a plane orthogonal to the vessel. Obtaining this from a 3D segmentation without temporal information might introduce errors, since the vessel pulsation is neglected. Manual contour drawing can be carried out by the user. However, this is tedious if multiple evaluations are performed. Goel et al. [GMK\*14] described an automatic method to find vessel cross-sections in the anatomy image. They perform an edge detection on 2D image slices and use a *Hough transform* to determine the most circular objects in each temporal position. Van Pelt et al. [VPBB\*10] detected cross-sections in the TMIP based on an *eigen-decomposition* of a local structure tensor. The results were used as seeding planes for the subsequent blood flow visualization.

## 4 Anatomical Context Visualization

The vessel anatomy can be visualized using *geometric surface meshes*, which are extracted from a 3D lumen segmentation (Sec. 3.2), or *direct volume rendering* (DVR) of a 3D high contrast image (Sec. 3.1). Both approaches are outlined in the following.

### 4.1 Geometric Surface Meshes

*Marching cubes* can be employed to extract triangular surface meshes from segmentations. If different vascular structures have separate meshes, single vessels can easily be hidden to focus the evaluation or reduce visual clutter. Mesh-based rendering techniques can be applied to create appealing visualizations. A common way to make intravascular

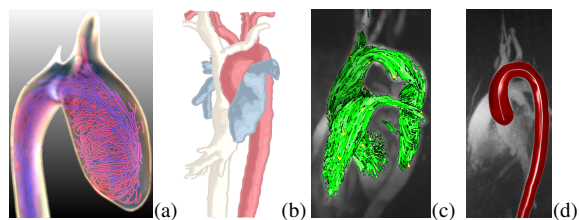


Figure 5: Anatomy visualization with surface meshes (a, b) and direct volume rendering, more precisely, maximum intensity projection (c, d). (a) A ghosted viewing of the culled vessel front emphasizes the shape perception. (b) Cel shading. (c) Flow provides an impression of the vessel shape. (d) Combined geometric surface and direct volume rendering.

flow visible is to render only the vessel's back side. Gasteiger et al. [GNKP10] use a *Fresnel-reflection model* to show parts of the culled front faces to increase the spatial shape perception: the smaller the angle between a surface normal and the view vector, the higher the transparency. Lawonn et al. [LGP14] additionally emphasize convex and concave regions with an illustrative technique that was inspired by *suggestive contours* (Fig. 5a). The method is applicable to arbitrary surfaces and thus suitable for the cardiac anatomy. Van Pelt et al. [VPBB\*10] abstract the surface depiction using a *cel shading* (Fig. 5b). Preim et al. [PB13] provide an overview of visualization of vascular structures.

### 4.2 Direct Volume Rendering

A DVR can be realized with *GPU raycasting*. The TMIP might be most suitable, since it shows the least noise. Unfortunately, viewing the internal flow is limited in standard DVR, since it is not simply possible to solely make the back side of the vessel opaque and the front as well as inner regions transparent. Methods that simulate isosurface visualizations by emphasizing boundaries could use gradients to approximate front face culling. However, a common approach is to employ a maximum intensity projection (MIP). This avoids unnecessary algorithm complexity and the specification of a transfer function. Due to the 2D nature of MIP, spatial relations get lost. However, when intravascular flow is shown, the user gets a reasonable impression of the vessel shape (Fig. 5c). Venkataraman [Ven10] implemented such an approach as technical demo. A MIP is also suitable for the combination with a geometric mesh, since it can be used as background for the vessel surface rendering. (Fig. 5d).

## 5 Qualitative Flow Analysis

Analysis of the vessel shape helps to assess morphology-related pathologies such as dilations or narrowings. However, the investigation of blood flow characteristics facilitates a deeper understanding. Inspired by Post et al. [PVH\*03], we explain direct as well as geometry- and feature-based flow visualization techniques in the following.

### 5.1 Direct Methods

These techniques directly visualize the underlying flow data. They are suitable to illustrate basic flow characteristics in the vessel cross-section, whereas 3D and 4D visualizations are dominated by visual clutter.

**Velocity Profile.** Blood flow through a cross-section is often color-coded according to the velocities. The temporal development of the flow profile might be shown in an animation or as height field (Fig. 6a). This allows to manually draw conclusions on the distribution of high velocities. Line or arrow *glyphs* can be helpful to analyze flow patterns in a cross-section (Fig. 6b).

**Flow DVR.** A DVR (Sec. 4.2) of flow velocities in one time step illustrates the distribution of fast and slow blood (Fig. 6c). Masking (Sec. 3.2) the phase images is recommended to exclude surrounding noise from the visualization.



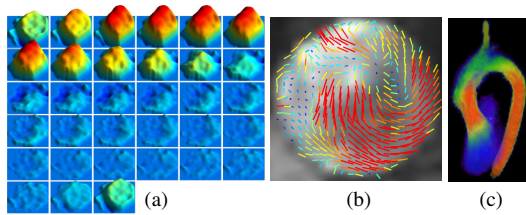


Figure 6: Direct visualization techniques. (a) Time-varying flow profile as height field. (b) Flow pattern in a cross-section via line glyphs. (c) DVR of systolic flow velocities.

## 5.2 Geometry-based Methods

Techniques from this group depict the course of blood flow trajectories via geometric objects such as lines.

**Path Calculation.** The common approach to calculate blood flow trajectories is to use an integration scheme from the *Runge Kutta* family such as *DOPRI5(4)* [DP80]. This is suitable for GPU computing and thus very fast. If only one temporal position is considered, the integration yields a 3D *streamline*. However, only a 4D (3D+time) *pathline* (also: *particle path*) represents a blood flow trajectory in the cardiac cycle. Pathlines can be precalculated in an initialization step, which increases the performance during the visualization (or animation). Another approach is to perform the flow integration in real-time as particle system, where each particle stores a series of recent positions. Seeding positions can be distributed uniformly within the vessel or in an estimated mask of features.

**Visualization.** Particles may be visualized as spheres, as ellipsoids that are stretched according to the flow velocity [VPBB\*11] or as cones [KGP\*13] (Fig. 7a). *Pathlets* (also: *trails*) emphasize the development of a trajectory. Temporal information can be mapped to transparency, so that the opacity is decreased for older positions. In this case, *order independent transparency* [YHGT10] is recommended to ensure correct alpha blending.

The geometries of pathlets can be shown all at once without employing the temporal information. Techniques such as *illuminated streamlines* and *halos* [MLP\*10] are suitable at this point to enhance the flow visualization. If (semi-)quantitative assessment is the focus, a careful use of line visualization techniques is recommended to avoid distractions (Fig. 7b). A pathlet visualization can also be achieved with precalculated pathlines. Particles (the glyphs) are placed at positions where the current time of the running animation matches the temporal component of the pathline. In addition, only a small time frame around the particle position is shown, i.e., all pathline points with a temporal distance higher than a threshold are hidden.

**Interaction.** Manipulation of the current animation time is possible with a slider or simply via pause/stop/play. An advantage of precalculated pathlines over on-the-fly-integrated particles is that the exact same paths can be evaluated multiple times. Vilanova et al. [VPvP\*14] provide an overview of further exploration tools for measured or simulated, cerebral or cardiac data.

**Simplification.** Visual clutter is a problem for dense line sets. Born et al. [BMGS13] addressed this problem by creating 3D arrows as representatives of line bundles (Fig. 7c). Van Pelt et al. [VPJtHRV12] performed a hierarchical clustering on the phase images and generated a representative pathline for each cluster. Angelelli et al. [AH11] described a vessel straightening to simplify side-by-side visualizations of integral lines of different temporal positions.

## 5.3 Feature-based Methods

Feature extraction is used to simplify visualizations or to answer specific questions. E.g., high-velocity jets in cardiac vessels are of great clinical interest or vortical flow, since this is considered as indicator for different pathologies.

**Line Predicates.** Salzbrunn et al. [SGSM08] introduced *line predicates* as Boolean functions that decide if integral lines such as pathlines fulfill certain properties of interest. The filtering criteria are based on line geometries, the underlying flow field or mesh-related measures such as distances to the vessel wall. A predicate can be applied to whole lines or to the single points of it. In the latter case, lines can be split into fragments. However, different predicates can be concatenated with common set operations in order to formulate complex queries. Shi et al. [STH\*09] described various attributes especially for pathlines. Born et al. [BPM\*13] used line predicates to extract different features such as specific flow paths, jets (Fig. 7d) or blood with high *residence times*. Further, they extracted vortices and used predicates to display involved integral lines. Gasteiger et al. [GLvP\*12] determined *inflow jets* and *impingement zones* in simulated (CFD) blood flow data of cerebral aneurysms, which shows the high flexibility of line predicates.

**Vortex Cores.** The majority of methods from the flow analysis community is made for 2D or 3D vector fields and thus not directly applicable for 4D PC-MRI data. Evaluating each temporal position independently with a 3D method

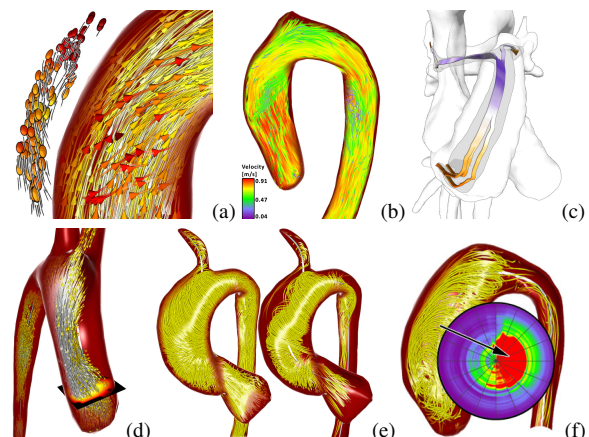


Figure 7: Trajectories are visualized as pathlets (b) with ellipsoids or cones (a) as particles. (c) 3D arrows as representatives of line bundles. (d) Extracted systolic inflow jet. (e) Before and after vortex extraction. (f) 2D polar plot as overview of aortic vortex flow.

might introduce errors, since it is not guaranteed that vortices of streamlines and pathlines coincide. Stalder et al. [SFH\*10] used a combination of the  $\lambda_2$  criterion and the *reduced velocity* (overview by Jiang et al. [JMT05]) to identify independent points that represent vortex cores mainly in the aorta. Streamlines were seeded in the close surrounding to provide a visual impression of the vortices. Elbaz et al. [ECW\*14] employed the  $\lambda_2$  criterion to extract vortex core rings, which are assumed to be a blood transport mechanism in the left ventricle. However, vortex core extraction is challenging due to noise in the measured data.

**Vortex Regions.** According to the observations of Köhler et al. [KGP\*13], clinicians are often more interested in the characteristic of a vortex than topological properties such as core lines. Consequently, they aimed at extracting visually appealing pathlines with long, continuous and smooth courses (Fig. 7e). They incorporated different local vortex criteria in the line predicates technique and determined the  $\lambda_2$  criterion as most suitable. Carnecky et al. [CBW\*14] further increase noise robustness of the  $\lambda_2$  calculation by suggesting an orthogonal decomposition of the phase images. The vortex representing pathlines were used to establish a polar plot [KMP\*15] that shows present vortex flow in the aorta at one glance (Fig. 7f). The temporal component is mapped to the angle, analogous to a clock, and the course of the centerline is mapped to the radius, starting at the aortic valve location in the center.

**Planar Flow Patterns.** Heiberg et al. [HEWK03] described *vector pattern matching* (VPM). They analyze the similarity of normalized flow vectors in a plane (Fig. 6b) to six idealized templates, such as right-handedly swirling flow, via convolution. The largest eigenvalue of the resulting structure tensor per voxel is used as similarity measure. The computational effort is high, since different rotations of the 2D patterns are used to find the maximum similarity. Furthermore, specification of the templates requires a priori knowledge, e.g., about the forward movement (axial velocity) along the vortex core. Drexler et al. [DKM\*13] proposed an adaptive VPM, where candidate voxels are identified using a threshold on the *vorticity* magnitude. The vortex core orientation is then estimated with the vorticity vector and templates are rotated accordingly. Van Pelt et al. [VPFCV14] proposed a VPM-based blood flow characterization. They define a single parameter  $\in [0, 1]$  that is sufficient to describe patterns in the plane.

## 6 Quantification

Quantitative measures are essential to assess the severity of pathologies or to support treatment decisions. Hope et al. [HSD13] provide an overview of different measures with emphasis on the clinical importance, whereas we focus on the calculation in this section.

### 6.1 Cross-sectional Methods

Measuring planes that are modeled as discrete grid are the basis for many quantifications. An accurate determination

of the lumen pixels is required (Sec. 3.3). A plane can be aligned orthogonally to the vessel using the centerline direction, if available, or via time-averaged flow vectors as estimation of the vessel course. Measuring planes can be evaluated at arbitrary positions, which might impede result comparison between different datasets. As a remedy, equidistant planes starting from a specific location such as the aortic valve could be used or evaluation at certain landmarks such as branching vessels.

**Flow Rate.** The time-dependent *flow rate*  $fr(t)$  [ml/s] describes the orthogonally passing blood flow through a plane  $P$  with the normal vector  $\vec{n} \in \mathbb{R}^3$ , scale  $\vec{s} \in \mathbb{R}^2$  [mm<sup>2</sup>] per cell and grid size  $\vec{g} \in \mathbb{N}^2$ :

$$fr(t) = s_x \cdot s_y \cdot \vec{n} \cdot \sum_{x=0}^{g_x-1} \sum_{y=0}^{g_y-1} S(P(x,y),t) \cdot V(P(x,y),t) \quad (5)$$

$$\text{with } S(P(x,y),t) = \begin{cases} 1, & P(x,y),t \text{ inside vessel} \\ 0, & \text{else} \end{cases}$$

$P(x,y) = \vec{p}$  is a position on the plane transformed to world coordinates.  $V(\vec{p},t)$  [m/s] yields velocity vectors from the phase images. If calculated for each temporal position,  $fr(t)$  is periodic, since it represents one full heartbeat (Fig. 8a).

The *forward flow volume* (FFV) [ml] and *backward flow volume* (BFV) [ml] is the area of the curve above and below 0, respectively, scaled with  $10^{-3}$  to obtain [ml]. The *net flow volume* (NFV) [ml] is FFV – BFV or simply the integral of  $fr(t)$ . The *stroke volume* (SV) [ml] describes the pumped blood per heartbeat and thus helps to assess the cardiac function. It is a special case of the NFV, where the measuring plane is located directly above the aortic or pulmonary valve.

Hoogeveen et al. [HBV99] pointed out the susceptibility of the flow rate calculation to different imaging artifacts. They suggested a model-based approach that is applicable small, straight and cylindrical arteries with a parabolic velocity profile. Therefore, this is not suitable for the cardiac context. Köhler et al. [KPG\*15] determined vortex flow as a main cause for quantification uncertainties. They suggest a systematic evaluation of measuring planes with slightly different angulations, which yields a distribution of NFVs. A box plot-based graph illustrates the result variations.

**Pulse Wave Velocity.** The *pulse wave velocity* (PWV) [m/s] is an indicator for arterial stiffness, since it is lower and higher in elastic and stiff vessels, respectively. Wentland et al. [WGW14] provide an overview of MRI-based PWV measurements, Markl et al. [MWB\*10] focus on 4D PC-MRI. It is calculated as:

$$PWV = \frac{\Delta d}{\Delta t}, \quad (6)$$

where  $\Delta d$  [m] describes the intravascular distance (length of the centerline) between two measuring planes (Fig. 8c).  $\Delta t$  [s] is the temporal offset of the flow rate  $fr(t)$  curves. Landmarks are determined for each curve, then the offset is derived (Fig. 8d). Solely using the curves' peaks as landmarks (*time-to-peak* (TTP) method) is prone to errors, since the actual peak can easily be missed due to the limited tem-

poral data resolution. Another approach is to fit a regression line to the upslope of the waveform and then determine its intersection with either the baseline ( $fr(t) = 0$ ) or another regression line prior to the upstroke (*time-to-foot* (TTF) method). More complex methods fit a *sigmoid function* or perform *cross-correlation* between the  $fr(t)$  curves. However, the PWV is often obtained using more than just two planes. In this case,  $\Delta d$  and  $\Delta t$  are calculated between each plane sample and the first plane. The inverse slope of a fitted regression line yields the PWV. Drexler et al. [DKM\*13] describe a PWV calculation, where the user simply defines a start and end position on the centerline and planes with equal distances  $\Delta s$  are generated and evaluated automatically.

**Flow Displacement.** The normally parabolic velocity profile can be disrupted by vortex flow patterns or disturbed valve opening characteristics. To quantify *eccentric flow jets*, Sigovan et al. [SDW\*15] define *flow displacement*  $\in [0, 1]$  in a cross-section as distance between the center position and the "center of velocities", which is the velocity-weighted average of all positions in the plane, normalized with the vessel diameter (Fig. 8b).

## 6.2 Surface-based Methods

Measures from this group are calculated for each position on the vessel surface.

**Wall Shear Stress.** WSS [Pa] represents the force tangential to the inner layer of the vessel wall caused by nearby complex blood flow. Papaioannou et al. [PS05] provide an overview. Recent research suggests that exposure to increased shear forces over a long period of time promotes pathologic vessel dilations (Fig. 8f). WSS is defined as:

$$\text{WSS}(t) = \mu \cdot \|\tau_{\vec{w}_{SS}}(t)\| \quad \text{with} \quad \tau_{\vec{w}_{SS}}(t) = \frac{\partial \vec{u}_t}{\partial \vec{n}^s}, \quad (7)$$

where  $\vec{n}^s$  is the normal vector of the corresponding surface mesh vertex  $s$ . The blood's dynamic viscosity  $\mu$  [Pa · s] describes the resistance to gradual deformation by shear stress:  $10^{-3} \cdot 3.5$  [PS05] or  $3.2$  [WSN10] are commonly chosen for large arteries.  $\tau_{\vec{w}_{SS}}(t)$  is the shear rate [1/s]. Velocity vectors  $V(\vec{p}_t)$  are obtained along the inward pointing normal with the number of samples as well as the maximum distance from the surface point  $s$  as parameters. An orthonormal basis  $\{\vec{n}^s, \vec{n}_x^s, \vec{n}_y^s\}$  is used to obtain  $\vec{u}_t = (V(\vec{p}_t) \cdot \vec{n}_x^s, V(\vec{p}_t) \cdot \vec{n}_y^s)^T$  that are parallel to the surface's tangential plane. The first derivatives  $\tau_{\vec{w}_{SS}}(t)$  of the  $\vec{u}_t$  samples are calculated analytically and evaluated at the vessel wall [PVOVN12, VOPG\*13] (Fig. 8e). One-dimensional, interpolating cubic b-splines with natural boundary conditions can be fitted to the x and y component of  $\vec{u}_t$  for this purpose.

Two common approaches are to calculate the *time-averaged* WSS or to focus on *peak-systolic* values. It has been shown that WSS peak locations obtained from simulated CFD and measured 4D PC-MRI data coincide well, but absolute values differ greatly, mainly caused by the limited spatial resolution of the measured data.

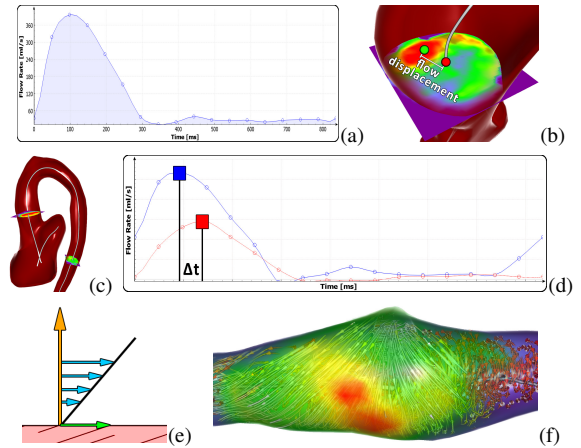


Figure 8: Quantification methods. (a) Flow rate curve from a measuring plane in the ascending aorta of a healthy volunteer. (b) Flow displacement in a cross-section as difference between the center position (red) to the "center of velocities" (green). (c, d) Temporal offset of the flow curve between measuring planes in the ascending and descending aorta. Images based on Wentland et al. [WGW14]. (e) Velocity vectors (blue) that are sampled along the normal (orange) are used to obtain the wall shear stress vector (green) on the vessel surface (red). (f) Flow impinges on the vessel wall and causes increased shear forces.

## 6.3 Grid-based Methods

Techniques from this group operate directly on the acquired image data or solve *differential equations* in *finite elements*.

**Pressure.** In case of narrowed (*stenotic*) vessels or valves, blood has to pass a smaller cross-sectional area or valve orifice. Increased flow velocities and intravascular pressure are the consequence. Thus, the blood's *relative pressure*  $p$  [mmHg] is an important factor to grade the degree of stenosis. In viscous, incompressible fluids such as blood it can be derived using the *Pressure Poisson equation* (PPE), which is based on the *Navier-Stokes equation*:

$$-\Delta p = \nabla \cdot \left( \rho \cdot \frac{\partial \vec{v}}{\partial t} + \rho \cdot (\vec{v} \cdot \nabla) \cdot \vec{v} - \mu \cdot \nabla^2 \vec{v} \right) \quad (8)$$

The divergence-free condition  $\nabla \cdot \vec{v} = 0$  must be met due to the fluid incompressibility.  $\rho = 1060$  [kg/m<sup>3</sup>] is the fluid density [BFL\*11],  $\mu = 10^{-3} \cdot 3.5$  [Pa · s] is the *dynamic viscosity*,  $\vec{v}$  [m/s] are velocity vectors from the phase images and  $t$  [s] is the time. Gravitational forces can be neglected due to the horizontal patient positioning in the scanner.

Tyszka et al. [TLAS00] described an *iterative PPE solver*. Ebbers and Farnebäck [EF09] proposed a *multi-grid finite-difference scheme* to solve the PPE directly in the segmented vessel, which respects physically correct boundary conditions, which respects physically correct boundary conditions. Meier et al. [MHF\*10] exploit properties of hexahedral voxel grid elements in order to simplify the incorporation of these boundary conditions and being able to use efficient conjugate solvers due to a symmetric system matrix. Lamata et al. [LKN\*14] describe a separate evaluation



of the transient  $\rho \cdot \frac{\partial \vec{v}}{\partial t}$ , convective  $\rho \cdot (\vec{v} \cdot \nabla) \cdot \vec{v}$  and viscous component  $-\mu \cdot \nabla^2 \vec{v}$  (Eq. 8). They identified transient effects, which originate from the acceleration of the blood, as main cause for relative pressure in the aorta.

**Turbulent Kinetic Energy.** Flow turbulences are irregularities and a certain randomness of the blood flow. Dyverfeldt et al. [DKS\*08] describe *turbulent kinetic energy* (TKE) [ $\text{J}/\text{m}^3$ ] as direction-independent measure of turbulence intensities. A *Reynolds decomposition* of the velocity field  $V$ , given by the phase images, yields a separation into a mean  $\bar{V}$  and fluctuating velocity field  $V'$ , so that  $V = \bar{V} + V'$ . Assuming a Gaussian distribution, the kinetic energy of the velocity fluctuations (the TKE) corresponds to:

$$\text{TKE} = \frac{\rho}{2} \cdot \sigma^2, \quad (9)$$

where  $\sigma^2$  [ $\text{m}^2/\text{s}^2$ ] is the variance of velocities and  $\rho$  [ $\text{kg}/\text{m}^3$ ] is the fluid density [BKM\*13]. An elevated level of TKE increases the heart's workload and thus might enhance the risk of ventricular hypertrophy (enlargement).

**Lagrangian Coherent Structures.** LCSs facilitate the creation of surfaces, e.g., at vortex boundaries, that divide flow into regions with different characteristics. Based on this, Töger et al. [TKC\*12] established a volume quantification of vortex rings (recall Sec. 5.3).

LCSs are based on *finite-time Lyapunov exponents* (FTLE), which describe the rate of separation of nearby particles when integrated for a certain time frame  $\Delta t$ . A *flow map*, usually with a higher resolution than the acquired image data, contains the end positions of particles that started at the spatio-temporal positions  $\vec{p}_{t_0}$  and were integrated for  $\Delta t$ . The FTLE is defined as:

$$\text{FTLE}(\vec{p}_{t_0}) = \frac{1}{\Delta t} \cdot \log(\lambda(\vec{p}_{t_0})) \quad (10)$$

$$\text{with } \lambda(\vec{p}_{t_0}) = \sqrt{\lambda_{\max}[J(\vec{p}_{t_0})^T \cdot J(\vec{p}_{t_0})]}$$

$J$  is the Jacobian matrix and  $\lambda_{\max}$  the maximum eigenvalue. Krishnan et al. [KGG\*12] directly employ the FTLE as a stop criterion for particle path calculations (Sec. 5.2). If the FTLE is determined close to the vessel boundaries, some of the nearby particles will be seeded inside and some will be placed outside the vessel. Thus, some particles follow the intravascular flow and some will experience a "random" movement due to low velocities and/or arbitrary directions outside the vessel. The resulting high separation allows to estimate the vessel boundaries via thresholding.

**Connectivity Uncertainty.** Friman et al. [FHH\*10] introduced a probabilistic approach that employs a sequential *Monte Carlo* sampling to quantify and visualize uncertainties in the integration. Schwenke et al. [SHFF11] incorporate an estimated uncertainty tensor into a *fast marching* method and calculate blood flow trajectories as minimal paths.

## 7 Concluding Remarks

4D PC-MRI enables the measurement of 3D blood flow and its change over the heart cycle. Medical researchers start using these data to develop an increased understanding of

healthy cardiovascular systems and to find indicators for the genesis and evolution of CVDs. 4D PC-MRI is expected to significantly improve patient treatment, which is confirmed by recent medical studies [CRvdG\*14, SAG\*14]. A long-term goal is to obtain age- and gender-specific normative values for different flow parameters, which could help to refine current treatment guidelines. However, data in itself are not sufficient for significant medical progress. Until now, 4D PC-MRI is mainly used for research purposes, among others, due to a lack of standardized and easy-to-use evaluation software with guided workflows and an automated report generation. Various free or commercial tools already exist or are being developed such as *FourFlow* [HGT\*12], *Bloodline* [KPG\*15], *Quantitative Flow Explorer* [VPBB\*10], *MeVisFlow* [HFS\*11], *GTFlow*, *QFlow ES*, *CMR 42*, *Arterys*, *Siemens 4D Flow Demonstrator* [SCG\*14] and *EnSight*. An overview of arising visualization challenges is given by Van Pelt et al. [VPV13]. In this survey, we presented the state-of-the-art of quantitative and qualitative 4D PC-MRI data analysis and visualization to give a starting point for further advancements, which facilitate the evaluation of larger studies and make 4D PC-MRI viable for the clinical routine.

## Acknowledgements

We would like to thank Anja Hennemuth (Fraunhofer MEVIS) for valuable feedback.

## References

- [AH11] ANGELELLI P., HAUSER H.: Straightening tubular flow for side-by-side visualization. *IEEE TVCG* 17, 12 (2011), 2063–70. 5
- [BFL\*11] BOCK J., FRYDRYCHOWICZ A., LORENZ R., HIRTLE D., BARKER A. J., JOHNSON K. M., ARNOLD R., BURKHARDT H., HENNIG J., MARKL M.: In vivo noninvasive 4D pressure difference mapping in the human aorta: Phantom comparison and application in healthy volunteers and patients. *JMRI* 66, 4 (2011), 1079–88. 7
- [BKHM07] BOCK J., KREHER B., HENNING J., MARKL M.: Optimized pre-processing of time-resolved 2D and 3D phase contrast MRI data. In *Proc ISMRM* (2007), p. 3138. 2
- [BKM\*13] BINTER C., KNOBLOCH V., MANKA R., SIGFRIDSSON A., KOZERKE S.: Bayesian multipoint velocity encoding for concurrent flow and turbulence mapping. *JMRM* 69, 5 (2013), 1337–45. 8
- [BMGS13] BORN S., MARKL M., GUTBERLET M., SCHEUERMANN G.: Illustrative visualization of cardiac and aortic blood flow from 4D MRI data. In *Proc IEEE PacificVis* (2013), pp. 129–36. 5
- [BPM\*13] BORN S., PFEIFLE M., MARKL M., GUTBERLET M., SCHEUERMANN G.: Visual analysis of cardiac 4D MRI blood flow using line predicates. *IEEE TVCG* 19 (2013), 900–12. 5
- [BVP\*13] BOSTAN E., VARDOULIS O., PICCINI D., TAFTI P. D., STERGIOPULOS N., UNSER M.: Spatio-temporal regularization of flow-fields. In *Proc IEEE ISBI* (2013), pp. 824–7. 3
- [BWJ\*08] BOCK J., WIEBEN O., JOHNSON K., HENNIG J., MARKL M.: Optimal processing to derive static PC-MRA from time-resolved 3D PC-MRI data. In *Proc ISMRM* (2008), p. 3053. 3
- [CBW\*14] CARNECKY R., BRUNNER T., BORN S., WASER J., HEINE C., PEIKERT R.: Vortex detection in 4D MRI data: Using the proper orthogonal decomposition for improved noise-



- robustness. In *Proc EuroVis Short Papers* (2014), pp. 127–31. 6
- [CNS04] CHUNG A. C. S., NOBLE J. A., SUMMERS P.: Vascular segmentation of phase contrast magnetic resonance angiograms based on statistical mixture modeling and local phase coherence. *IEEE TMI* 23, 12 (2004), 1490–507. 3
- [CRvdG\*14] CALKOEN E. E., ROEST A. A. W., VAN DER GEEST R. J., DE ROOS A., WESTENBERG J. J. M.: Cardiovascular function and flow by 4-dimensional magnetic resonance imaging techniques: New applications. *JTI* 29, 3 (2014), 185–96. 1, 8
- [CSCW07] CHERNOBELSKY A., SHUBAYEV O., COMEAU C. R., WOLFF S. D.: Baseline correction of phase contrast images improves quantification of blood flow in the great vessels. *JCMR* 9, 4 (2007), 681–5. 2
- [DKM\*13] DREXL J., KHAN H., MARKL M., HENNEMUTH A., MEIER S., LORENZ R., HAHN H. K.: Detection of vortical structures in 4D velocity encoded phase contrast MRI data using vector template matching. In *Proc FIMH*. 2013, pp. 276–83. 6, 7
- [DKS\*08] DYVERFELDT P., KVITTING J. P., SIGFRIDSSON A., ENGVALL J., BOLGER A. F., EBBERS T.: Assessment of fluctuating velocities in disturbed cardiovascular blood flow: In vivo feasibility of generalized phase-contrast MRI. *JMRI* 28, 3 (2008), 655–63. 8
- [DP80] DORMAND J. R., PRINCE P. J.: A family of embedded runge-kutta formulae. *JCAM* 6, 1 (1980), 19–26. 5
- [DR04] DÍAZ C., ROBLES L. A.: Fast noncontinuous path phase-unwrapping algorithm based on gradients and mask. In *Proc CIARP* (2004), pp. 116–23. 2
- [ECW\*14] ELBAZ M. S. M., CALKOEN E. E., WESTENBERG J. J. M., LELIEVELDT B. P. F., ROEST A. A. W., VAN DER GEEST R. J.: Vortex flow during early and late left ventricular filling in normal subjects: Quantitative characterization using retrospectively-gated 4D flow cardiovascular magnetic resonance and three-dimensional vortex core analysis. *JCMR* 16, 78 (2014), 12. 6
- [EF09] EBBERS T., FARNEBÄCK G.: Improving computation of cardiovascular relative pressure fields from velocity MRI. *JMRI* 30, 1 (2009), 54–61. 7
- [FGG\*13] FAIR M., GATEHOUSE P. D., GREISER A., DRIVAS P., FIRMIN D. N.: A novel approach to phase-contrast velocity offset correction by in vivo high-SNR acquisitions. *JCMR* 15, Suppl 1 (2013), P56. 2
- [FHH\*10] FRIMAN O., HENNEMUTH A., HARLOFF A., BOCK J., MARKL M., PEITGEN H.-O.: Probabilistic 4D blood flow mapping. In *Proc MICCAI* (2010), pp. 416–23. 8
- [GLvP\*12] GASTEIGER R., LEHMANN D. J., VAN PELT R. F. P., JANIGA G., BEUING O., VILANOVA A., THEISEL H., PREIM B.: Automatic detection and visualization of qualitative hemodynamic characteristics in cerebral aneurysms. *IEEE TVCG* 18, 12 (2012), 2178–87. 5
- [GMK\*14] GOEL A., MCCOLL R., KING K. S., WHITTEMORE A., PESHOCK R. M.: Fully automated tool to identify the aorta and compute flow using phase-contrast MRI: Validation and application in a large population based study. *JMRI* 40, 1 (2014), 221–8. 4
- [GNKPI0] GASTEIGER R., NEUGEBAUER M., KUBISCH C., PREIM B.: Adapted surface visualization of cerebral aneurysms with embedded blood flow information. In *Proc EG VCBM* (2010), pp. 25–32. 4
- [GT10] GÜLSÜN M. A., TEK H.: Segmentation of carotid arteries by graph-cuts using centerline models. In *Proc SPIE* (2010), p. 762530. 3
- [HBV99] HOOGEVEEN R. M., BAKKER C. J., VIERGEVER M. A.: MR phase-contrast flow measurement with limited spatial resolution in small vessels: Value of model-based image analysis. *JMRM* 41, 3 (1999), 520–8. 6
- [HEWK03] HEIBERG E., EBBERS T., WIGSTRÖM L., KARLSSON M.: Three-dimensional flow characterization using vector pattern matching. *IEEE TVCG* 9, 3 (2003), 313–9. 6
- [HFS\*11] HENNEMUTH A., FRIMAN O., SCHUMANN C., BOCK J., DREXL J., HUELLEBRAND M., MARKL M., PEITGEN H.-O.: Fast interactive exploration of 4D MRI flow data. In *Proc SPIE* (2011), pp. 79640E–11. 3, 8
- [HGT\*12] HEIBERG E., GREEN C., TÖGER J., ANDERSSON A. M., CARLSSON M., ARHEDEN H.: FourFlow - Open source code software for quantification and visualization of time-resolved three-directional phase contrast magnetic resonance velocity mapping. *JCMR* 14, Suppl 1 (2012), W14. 8
- [HSD13] HOPE M. D., SEDLIC T., DYVERFELDT P.: Cardiothoracic magnetic resonance flow imaging. *J Thorac Imag* 28, 4 (2013), 217–30. 6
- [JMT05] JIANG M., MACHIRAJU R., THOMPSON D.: Detection and visualization of vortices. In *The Vis Handbook* (2005), pp. 295–309. 6
- [KGG\*12] KRISHNAN H., GARTH C., GÜHRING J., GÜLSÜN M. A., GREISER A., JOY K. I.: Analysis of time-dependent flow-sensitive PC-MRI data. *IEEE TVCG* 18, 6 (2012), 966–77. 8
- [KGP\*13] KÖHLER B., GASTEIGER R., PREIM U., THEISEL H., GUTBERLET M., PREIM B.: Semi-automatic vortex extraction in 4D PC-MRI cardiac blood flow data using line predicates. *IEEE TVCG* 19, 12 (2013), 2773–82. 5, 6
- [KMP\*15] KÖHLER B., MEUSCHKE M., PREIM U., FISCHBACH K., GUTBERLET M., PREIM B.: Two-dimensional plot visualization of aortic vortex flow in cardiac 4D PC-MRI data. In *Proc BVM* (2015), pp. 257–61. 6
- [KPG\*15] KÖHLER B., PREIM U., GROTHOFF M., GUTBERLET M., FISCHBACH K., PREIM B.: Robust cardiac function assessment in 4D PC-MRI data of the aorta and pulmonary artery. *CGF*, to appear (2015). 3, 6, 8
- [LABFL09] LESAGE D., ANGELINI E. D., BLOCH I., FUNKALEA G.: A review of 3D vessel lumen segmentation techniques: Models, features and extraction schemes. *Med Imag Anal* 13, 6 (2009), 819–45. 3
- [LGP14] LAWONN K., GASTEIGER R., PREIM B.: Adaptive surface visualization of vessels with animated blood flow. *CGF* 33, 8 (2014), 16–27. 4
- [LHM\*05] LANKHAAR J.-W., HOFMAN M. B. M., MARCUS J. T., ZWANENBURG J. J. M., FAES T. J. C., VONK-NOORDEGRAAF A.: Correction of phase offset errors in main pulmonary artery flow quantification. *JMRI* 22, 1 (2005), 73–9. 2
- [LJLW11] LOECHER M., JOHNSON K., LANDGRAF B., WIEBEN O.: 4D gradient based phase unwrapping for PC-MR flow data. In *Proc ISMRM* (2011), p. 3284. 2
- [LKN\*14] LAMATA P. AND P. A., KRITTIAN S., NORDSLETTEN D., BISSELL M. M., CASSAR T., BARKER A. J., MARKL M., NEUBAUER S., SMITH N. P.: Aortic relative pressure components derived from four-dimensional flow cardiovascular magnetic resonance. *JMRM* 72, 4 (2014), 1162–9. 7
- [LMLG02] LOTZ J., MEIER C., LEPPERT A., GALANSKI M.: Cardiovascular flow measurement with phase-contrast MR imaging: Basic facts and implementation. *Radiographics* 22, 3 (2002), 651–71. 2
- [MFK\*12] MARKL M., FRYDRYCHOWICZ A., KOZERKE S., HOPE M. D., WIEBEN O.: 4D flow MRI. *JMRI* 36, 5 (2012), 1015–36. 2
- [MH15] MIRZAEI H., HENNEMUTH A.: Noninvasive measurement of intravascular pressure gradients based on 3D anatomy and 4D flow image fusion. In *Proc ISMRM* (2015), p. 2753. 3
- [MHE\*10] MEIER S., HENNEMUTH A., FRIMAN O., BOCK J., MARKL M., PREUSSER T.: Non-invasive 4D blood flow and pressure quantification in central blood vessels via PC-MRI. In *Proc Comput Cardiol* (2010), pp. 903–6. 7
- [MKE11] MARKL M., KILNER P. J., EBBERS T.: Comprehen-

- sive 4D velocity mapping of the heart and great vessels by cardiovascular magnetic resonance. *JCMR* 13, 7 (2011). 1
- [MLP\*10] MCLOUGHLIN T., LARAMEE R. S., PEIKERT R., POST F. H., CHEN M.: Over two decades of integration-based, geometric flow. *CGF* 29, 6 (2010), 1807–29. 5
- [MWB\*10] MARKL M., WALLIS W., BRENDENCKE S., SIMON J., FRYDRYCHOWICZ A., A. H.: Estimation of global aortic pulse wave velocity by flow-sensitive 4D MRI. *JMRM* 63, 6 (2010), 1575–82. 6
- [NJF\*12] NETT E. J., JOHNSON K. M., FRYDRYCHOWICZ A., DEL RIO A. M., SCHRAUBEN E., FRANCOIS C. J., WIEBEN O.: Four-dimensional phase contrast magnetic resonance imaging with accelerated dual velocity encoding. *JMRI* 35, 6 (2012), 1462–71. 2
- [OUT\*15] ONG F., UECKER M., TARIQ U., HSIAO A., ALLEY M. T., VASANAWALA S. S., LUSTIG M.: Robust 4D flow denoising using divergence-free wavelet transform. *JMRM* 73, 2 (2015), 828–42. 3
- [PB13] PREIM B., BOTHA C.: *Visual computing for medicine*, 2 ed. Morgan Kaufmann Publishers, 2013. 4
- [PS05] PAPAIOANNOU T. G., STEFANADIS C.: Vascular wall shear stress: Basic principles and methods. *HJC* 46, 1 (2005), 9–15. 7
- [PVH\*03] POST F. H., VROLIJK B., HAUSER H., LARAMEE R. S., DOLEISCH H.: The state of the art in flow visualisation: Feature extraction and tracking. *CGF* 22, 4 (2003), 775–92. 4
- [PVOVN12] POTTERS W. V., VAN OOIJ P., VANBAVEL E., NEDERVEEN A.: Vectorial wall shear stress calculations in vessel structures using 4D PC-MRI. *JCMR* 14, 1 (2012), W5. 7
- [SAG\*14] STANKOVIC Z., ALLEN B. D., GARCIA J., JARVIS K. B., MARKL M.: 4D flow imaging with MRI. *JCDT* 4, 2 (2014), 173–92. 1, 8
- [SCG\*14] SEMAAN E. M., CARR M., GÜLSÜN M. A., VAN OOIJ P., STALDER A. F., CARR J., COLLINS J., MARKL M., SPOTTISWOODE B.: Evaluation of an optimized post-processing tool for 4D flow MRI data analysis in healthy volunteers and patients with aortic stenosis, aortic insufficiency, and aortic aneurysm. In *Proc ISMRM* (2014), p. 3948. 8
- [SDW\*15] SIGOVAN M., DYVERFELDT P., WRENN J., TSENG E. E., SALONER D., HOPE M. D.: Extended 3D approach for quantification of abnormal ascending aortic flow. *JMRI* 33, 5 (2015), 695–700. 7
- [SFH\*10] STALDER A., FRYDRYCHOWICZ A., HARLOFF A., YANG Q., BOCK J., HENNIG J., LI K. C., MARKL M.: Vortex core detection and visualization using 4D flow-sensitive MRI. In *Proc ISMRM* (2010). 6
- [SGGJ13] STALDER A. F., GÜLSÜN M. A., GREISER A., JOLLY M.-P.: Fully automatic visualization of 4D flow data. In *Proc ISMRM* (2013), p. 1434. 3
- [SGSM08] SALZBRUNN T., GARTH C., SCHEUERMANN G., MEYER J.: Pathline predicates and unsteady flow structures. *The Visual Computer* 24, 12 (2008), 1039–51. 5
- [SHFF11] SCHWENKE M., HENNEMUTH A., FISCHER B., FRIMAN O.: Blood flow computation in phase-contrast MRI by minimal paths in anisotropic media. In *Proc MICCAI* (2011), pp. 436–43. 8
- [SHG\*06] SALFITY M. F., HUNTLEY J. M., GRAVES M. J., MARKLUND O., CUSACK R., BEAUREGARD D. A.: Extending the dynamic range of phase contrast magnetic resonance velocity imaging using advanced higher-dimensional phase unwrapping algorithms. *J Royal Soc Interface* 3, 8 (2006), 415–27. 2
- [SPH04] SOLEM J. E., PERSSON M., HEYDEN A.: Velocity based segmentation in phase contrast MRI images. In *Proc MICCAI* (2004), pp. 459–66. 3
- [STH\*09] SHI K., THEISEL H., HAUSER H., WEINKAUF T., MATKOVIC K., HEGE H.-C., SEIDEL H.-P.: Path line attributes - An information visualization approach to analyzing the dynamic behavior of 3D time-dependent flow fields. In *Proc Topol- Based Meth Vis II* (2009), pp. 75–88. 5
- [TKC\*12] TÖGER J., KANSKI M., CARLSSON M., KOVÁCS S. J., SÖDERLIND G., ARHEDEN H., HEIBERG E.: Vortex ring formation in the left ventricle of the heart: Analysis by 4D flow MRI and lagrangian coherent structures. *Ann Biomed Eng* 40, 12 (2012), 2652–62. 8
- [TLAS00] TYSZKA J. M., LAIDLAW D. H., ASA J. W., SILVERMAN J. M.: Three-dimensional, time-resolved (4D) relative pressure mapping using magnetic resonance imaging. *JMRI* 12, 2 (2000), 321–9. 7
- [Ven10] VENKATARAMAN S.: 4D visualization of cardiac flow, 2010. NVIDIA GPU Tech Conf Talk. 4
- [VOPG\*13] VAN OOIJ P., POTTERS W. V., GUÉDON A., SCHNEIDERS J. J., MARQUERING H. A., MAJOIE C. B., VANBAVEL E., NEDERVEEN A. J.: Wall shear stress estimated with phase contrast MRI in an in vitro and in vivo intracranial aneurysm. *JMRI* 38, 4 (2013), 876–84. 7
- [VPBB\*10] VAN PELT R. F. P., BESCOS J. O., BREEUWER M., RACHEL E. C., GRÖLLER M. E., TER HAAR ROMENY B. M., VILANOVA A.: Exploration of 4D MRI blood flow using stylistic visualization. *IEEE TVCG* 16, 6 (2010), 1339–47. 3, 4, 8
- [VPBB\*11] VAN PELT R. F. P., BESCÓS J. O., BREEUWER M., CLOUGH R. E., GRÖLLER M. E., TER HAAR ROMENY B. M., VILANOVA A.: Interactive virtual probing of 4D MRI blood-flow. *IEEE TVCG* 17, 12 (2011), 2153–62. 5
- [VPFCV14] VAN PELT R. F. P., FUSTER A., CLAASSEN G. G. H., VILANOVA A.: Characterization of blood-flow patterns from phase-contrast MRI velocity fields. In *EuroVis Short Papers* (2014). 6
- [VPJtHRV12] VAN PELT R. F. P., JACOBS S. S. A. M., TER HAAR ROMENY B. M., VILANOVA A.: Visualization of 4D blood-flow fields by spatiotemporal hierarchical clustering. *CGF* 31, 3 (2012), 1065–74. 5
- [VPNtHRV12] VAN PELT R. F. P., NGUYEN H., TER HAAR ROMENY B. M., VILANOVA A.: Automated segmentation of blood-flow regions in large thoracic arteries using 3D-cine PC-MRI measurements. *IJCARS* 7, 2 (2012), 217–24. 4
- [VPV13] VAN PELT R. F. P., VILANOVA A.: Understanding blood-flow dynamics: New challenges for visualization. *Computer* 46, 12 (2013), 60–7. 8
- [VPvP\*14] VILANOVA A., PREIM B., VAN PELT R. F. P., GASTEIGER R., NEUGEBAUER M., WISCHGOLL T.: *Visual exploration of simulated and measured blood flow*. Springer-Verlag London, 2014, ch. 25, pp. 305–20. 5
- [VTC\*15] VOLONGHI P., TRESOLDI D., CADIOLI M., USUELLI A. M., PONZINI R., MORBIDUCCI U., ESPOSITO A., RIZZO G.: Automatic extraction of three-dimensional thoracic aorta geometric model from phase contrast MRI for morphometric and hemodynamic characterization. *JMRM*, Epub ahead of print (2015). 4
- [WCS\*93] WALKER P. G., CRANNEY G. B., SCHEIDEGGER M. B., WASELESKI G., POHOST G. M., YOGANATHAN A. P.: Semiautomated method for noise reduction and background phase error correction in MR phase velocity data. *JMRI* 3, 3 (1993), 521–30. 2, 3
- [WGW14] WENTLAND A. L., GRIST T. M., WIEBEN O.: Review of MRI-based measurements of pulse wave velocity: A biomarker of arterial stiffness. *JCDT* 4, 2 (2014), 193–296. 6, 7
- [WSN10] WESTERHOF N., STERGIOPULOS N., NOBLE M. I. M.: *Snapshots of hemodynamics: An aid for clinical research and graduate education*. Springer, 2010. 7
- [WSW96] WIGSTRÖM L., SJÖQVIST L., WRANNE B.: Temporally resolved 3d phase-contrast imaging. *JMRI* 36, 5 (1996), 800–3. 1
- [YHGT10] YANG J. C., HENSLEY J., GRÜN H., THIBIEROZ N.: Real-time concurrent linked list construction on the GPU. In *CGF* (2010), pp. 1297–304. 5